A Comprehensive Characterization of Commercial Pulsed Laser Deposited Coated Conductors

Aixia Xu, Yan Xin, Dmytro Abraimov, *Member, IEEE*, Jin Gyu Park, Jan Jaroszynski, Fumitake Kametani, *Member, IEEE*, and David C. Larbalestier, *Life Fellow, IEEE*

***Abstract*—Comprehensive understanding is needed in order for the commercial pulsed laser deposited $REBa_2Cu_3O_{7-\delta}$ (RE: rare earth) coated conductors to be effectively used in the magnet and cable designs. Here we demonstrate the superconducting property characterization and microstructural analysis to show how different or similar the 3 commercial REBCO coated conductors are at present. Our work shows that the *ab*-plane of REBCO tilts from the coated conductor tape plane, leading to the offset of critical current density peak from the tape plane. In particular, the offset angle varies from less than 0.5° for one coated conductor to close to 5° for another. RE_2O_3 nanoparticles are dominant pins at 20 K and 15 T. The weak pinning introduced by RE_2O_3 particles and cation disorders contribute to critical current density at 20 K as well.**

***Index Terms*—REBCO coated conductor, pulsed laser deposition, critical current density, flux pinning.**

I. Introduction

$REBa_2Cu_3O_{7-\delta}$ (RE: rare earth, REBCO) coated conductors (CC) offer an opportunity to construct compact fusion energy reactors thanks to their exceptionally strong supercurrent carrying capability enabled by effective flux pinning engineering [1], [2]. The demonstration of the prototype 20 T toroidal magnet at 20 K by MIT and CFS demonstrated feasibility at large scale and large scale PLD CC manufacture [3]. Operation at 20 K and 20 T was only possible with REBCO CCs. Future construction of economically sustainable fusion energy reactors demands huge production of high performance REBCO CCs with price well below $50/kA-m [1], [4], [5].

Among all technologies for the REBCO conductor production, pulsed laser deposition (PLD) is being increasingly favored to achieve the fast production rate that is one of the key enablers for lowering the cost of REBCO CCs [6], [7]. At the industrial scale, the PLD REBCO CCs with attainable REBCO growth rate of 100 nm/s are commercially available from multiple manufacturers worldwide [4], [8], [9]. For pervasive REBCO CC adoption, intense R&D to bolster the growth rate and large volume production is being carried out under the strong collaborations between the industry and research institutes [10], [11], [12], [13].

Systematic comparison of recent commercial PLD REBCO CCs is beneficial for effective magnet and cable designs, and might be also valuable feedback for further optimization of REBCO production [14], [15], [16], [17]. However, such a comprehensive testing is not aways available even for the R&D samples and even fewer has been reported on commercial CCs. Here we present the comprehensive and systematic characterizations of the microstructure and pinning landscape of commercially available PLD REBCO CCs.

Received 1 October 2024; revised 24 December 2024; accepted 27 January 2025. Date of publication 7 February 2025; date of current version 21 February 2025. This work was supported by the U.S. Department of Energy, Office of Fusion Energy Sciences under Grant DE-SC0022011. This work was performed at the National High Magnetic Field Laboratory, which was supported in part by National Science Foundation Cooperative Agreements under Grant DMR-1644779 and Grant DMR-2128556, in part by the State of Florida, and in part by User Collaborations Grants Program Project #5217 under Grant DMR-1644779.
(Corresponding author: Aixia Xu.)

Aixia Xu, Yan Xin, Dmytro Abraimov, Jin Gyu Park, and Jan Jaroszynski are with National High Magnetic Field Laboratory, Florida State University, Tallahassee, FL 32310 USA (e-mail: aixiaxu@asc.magnet.fsu.edu).

Fumitake Kametani and David C. Larbalestier are with Applied Superconductivity Center, National High Magnetic Field Laboratory, Florida State University, Tallahassee, FL 32310 USA, and also with the Department of Mechanical Engineering, FAMU-FSU College of Engineering, Tallahassee, FL 32310 USA.
Color versions of one or more figures in this article are available at https://doi.org/10.1109/TASC.2025.3538638.

Digital Object Identifier 10.1109/TASC.2025.3538638

TABLE I
Key Parameter for 3 Selected PLD CCs

PLD CC	REBCO thickness (μm)	J_c (LN_2, sf) (MA/cm^2)	Transport T_c (K)
A	2.52	2.04	89.31
B	1.80	2.56	92.97
C	2.34	1.65	92.19

II. Experimental

Three 4 mm wide PLD CCs, purchased from 3 different CC manufacturers were selected. The selected CCs are denoted randomly as A, B, and C. A brief description of them is shown in Table I. REBCO layer thickness in Table I was measured on a CC cross section prepared by JEOL cross section polisher, using Zeiss 1540 EsB Scanning Electron Microscope (SEM). Critical current density J_c at liquid nitrogen temperature, $J_c(LN_2, sf)$, was measured on a full width CC in liquid nitrogen bath, and transport critical temperature T_c was measured on a ~40 μm wide bridge without any background field. It worth noting that the temperature of liquid nitrogen bath is ~77.6 K at our lab.

Magnetic moment M was measured from the temperature dependence of the warming magnetization under 1 mT perpendicular to the tape plane, in a Quantum Design MPMS-5 superconducting quantum interference device (SQUID) magnetometer. Magnetization T_c was defined as the onset temperature

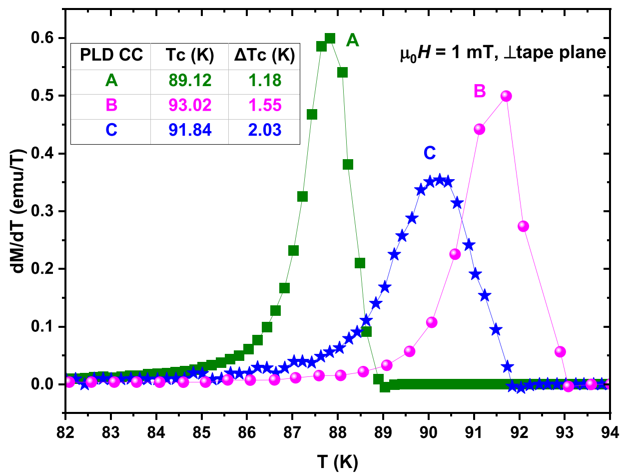

Fig. 1. First order derivative of moment M to temperature T, to emphasize the transition width. A shows lowest T_c, however sharpest transition. In comparison with B, C shows lower T_c and broader transition. The inset summarizes onset T_c value at $M = 0$, and T_c transition width defined as full width at half maximum.

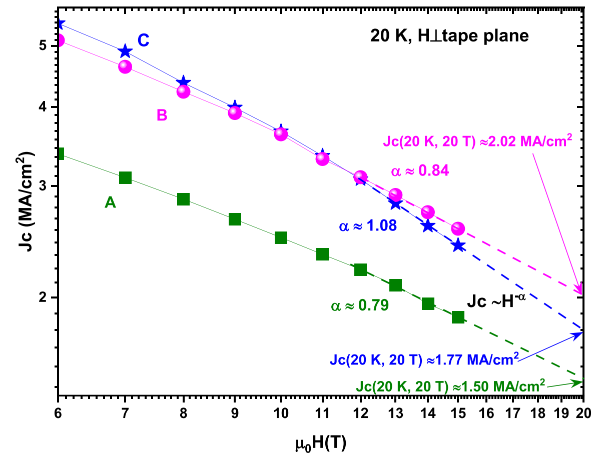

Fig. 2. Double-logarithmic plot for $J_c(H//c)$ at 20 K to highlight $J_c \propto H^{-\alpha}$, for which α increases from $\sim$0.79 for A to $\sim$0.84 for B and then to $\sim$1.08 for C. Extrapolated from power law, J_c(20 K, 20 T) is $\sim$1.50, $\sim$2.02 and $\sim$1.77 MA/cm^2 for A, B and C, respectively.

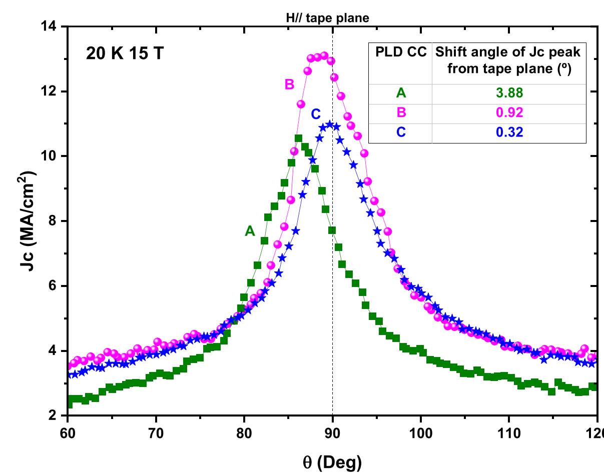

Fig. 3. $J_c(\theta)$ at 20 K and 15 T measured using the magneto torque probe. All 3 CCS show shifted $J_c(\theta)$ peaks from the tape plane. The inset lists shift angle values.

until $M = 0$. Transport J_c at 20 K and fields normal to the tape plane were measured using a home-made high current probe equipped with a variable temperature enclosure in a 15 T superconducting magnet (Oxford, U.K.) [18]. The angular dependent J_c, $J_c(\theta)$ was characterized using a magneto torque apparatus in a 16 T PPMS (Quantum Design USA) [19]. θ is defined as the angle between the applied field direction and the tape normal, for which $\theta = 90°$ is parallel to the tape plane.

X-ray diffraction (XRD) pole figure was carried out for texture analysis using a Rigaku SmartLab SE, with χ being the tilt angle relative to the tape length direction, and φ the rotation angle relative to the tape normal. Raman microscopy measurements were performed using a Renishaw System equipped with a He-Ne laser (633 nm). Cross-sectional Transmission Electron Microscope (TEM) samples were prepared by Focused Ion Beam (FIB) in a Thermo Fisher FEI Helios G4, followed by TEM imaging in a JEOL ARM200cF.

III. Results

Fig. 1 plots the first order derivative of moment M dependence on T, to highlight the superconducting transition. Coated conductor A shows T_c less than 90 K, and both B and C show T_c above 90 K. As shown in the inset table, T_c is $\sim$89.12 K for A, and $\sim$93.02 and $\sim$91.84 K for B and C, respectively. The superconducting transition width, ΔT_c, defined as the peak width at half maximum of dM/dT, $\sim$1.18 K for A, increases to $\sim$1.55 K for B and further to $\sim$2.03 K for C. Coated conductor B has clearly the highest T_c.

Fig. 2 presents the field-dependent J_c at 20 K from 6 to 15 T for field perpendicular to the tape plane. Coated conductors B and C are very similar in J_c and more than 30% higher than A. The plot is in double logarithmic scale to draw attention to the power law dependence of J_c, $J_c \propto H^{-\alpha}$. According to the power law fit from 12 to 15 T, the α value, $\sim$0.79 for A, increases to $\sim$0.84 for B, and then $\sim$1.08 for C. Also extrapolated from power law, J_c(20 K, 20 T) is $\sim$1.50, $\sim$2.02 and $\sim$1.77 MA/cm^2 for A, B and C, respectively. This variability of α may reflect the fact that at 20 K and 15 T the balance of vortex pinning between insulating strong pins and weak point pins is highly variable as thermal fluctuations depin the point defects such as cation disorders and oxygen defects [18], [20], [21].

Fig. 3 shows $J_c(\theta)$ at 20 K and 15 T for θ ranging from 60 to 120° that was measured by the torque magnetometer. Interestingly, the J_c peaks are markedly offset from the direction parallel to the tape plane, and the offset angle of each coated conductor quite varies. Conductor A shows the largest offset of $\sim$3.88°, while B and C are smaller at $\sim$0.93 and $\sim$0.32°, respectively. The peak J_c of B is $\sim$13.1 MA/cm^2, $\sim$20% higher than C ($\sim$11.0 MA/cm^2) and $\sim$24% higher than A ($\sim$10.6 MA/cm^2). Because of variable offset angles of J_c peak, J_c variation at H parallel to tape plane between these CCs appears much greater than the actual difference of peak J_c values. The difference of J_c at H parallel to tape plane is $\sim$16.8% between B and C, and $\sim$66.9% between B and A.

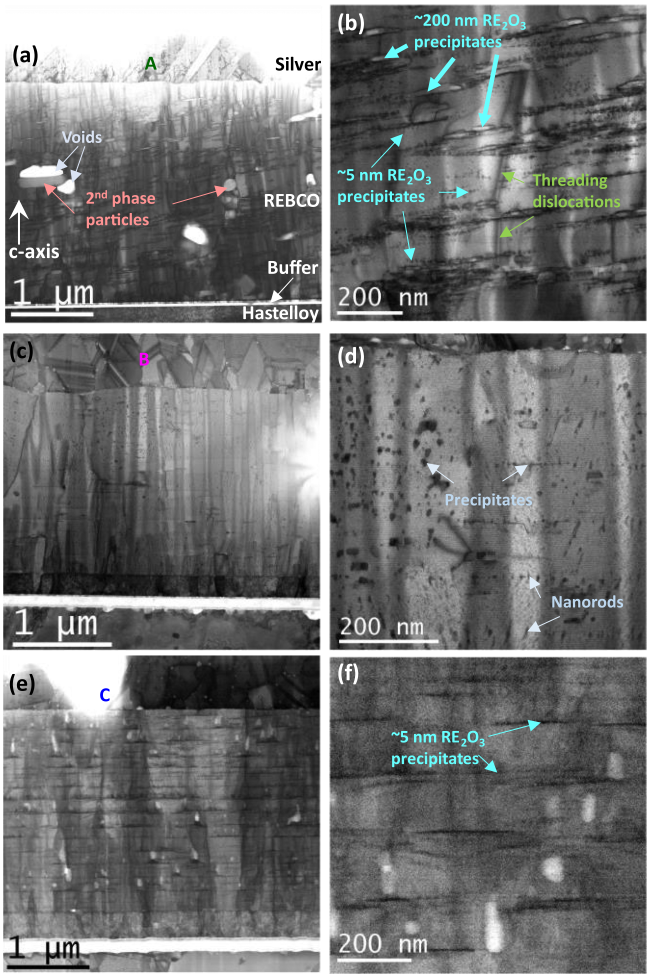

Fig. 4. Low magnification TEM images for (a) A, (c) B and (e) C displaying the overall REBCO layer microstructures, and high magnification TEM images for (b) A, (d) B and (f) C to highlight their pinning landscapes. The dominant flux pins in A and C are RE_2O_3 precipitate arrays lying along the *ab*-plane. Random precipitates and short *c*-axis splayed nanorods are additional pins in B. Voids were observed in A and C, and threading dislocations were observed in all 3 CCs.

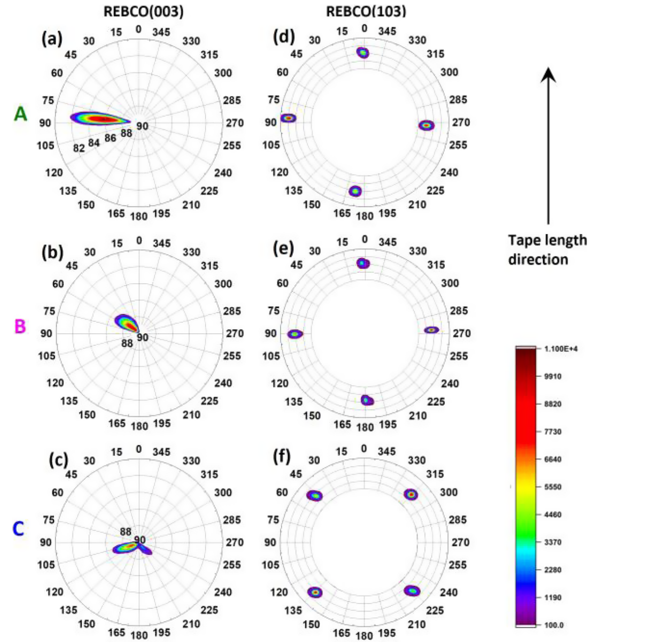

PLD CC	(003)		(103)	
	χ position (°)	FWHM along φ (°)	χ position (°)	FWHM along φ (°)
A	86.00	5.11	40.5	1.81
B	89.50	2.70	44.0	2.00
C	89.75	2.54	44.5	3.21

Fig. 5. REBCO (003) pole figures for (a) A, (b) B, and (c) C; and (103) pole figures for (d) A, (e) B, and (f) C. An obvious feature is the shift of the (003) peak from the pole figure center for all 3 CCs. An additional feature for C is the 45° rotation of (103) planes along the φ direction. As shown by the inset table, A exhibits better in-plane texture, while B and C show better out-of-plane texture.

Fig. 4 compares the TEM cross-section of those tapes. The low magnification TEM images of (a), (c) and (e) show the microstructure of entire REBCO layer. As marked in Fig. 4(a) as an example, the low magnification TEM captures the Ag layer right above the REBCO, under which the buffer layers and Hastelloy are also seen. The common features shared by all 3 PLD CCs are threading dislocations and the precipitate arrays. However, the morphology, size and distribution of precipitates strongly varies among the 3 CCs. The density of precipitates along the tape plane direction in A and C are much higher than in B. In A and C, in addition to the $\sim$5 nm RE_2O_3 precipitates which form the arrays along the *ab*-plane, A also contains larger RE_2O_3 precipitates of 100–200 nm in size. Such large precipitates that are pointed to by thick arrows in (b), tilt from the tape plane at an angle of $\sim$20°. On the other hand, the RE_2O_3 precipitates in C align more parallel to the tape plane [Fig. 4(e)]. The large RE_2O_3 is also present in C, but thinner than those in A. In B, the $BaHfO_3$ (BHO) precipitates are distributed uniformly without forming any clusters or arrays, although the density along the tape plane direction is smaller than A or C.

Another important feature observed from Fig. 4(a) and (e) are frequent voids in A and C. In C, the voids are approximately 20 nm in size and distributed rather uniformly in the REBCO layer. On the other hand, the voids in A are much bigger, $\sim$200–500 nm in size but distributed more sparsely. In contrast, voids are almost fully absent in B. Considering their size, we believed that such large voids and large precipitates found in A are both detrimental to J_c because they act as current-blocking, not vortex pinning defects.

High magnification TEM images of (b), (e), and (f) reveal the potential flux pins. The effective pins in A and C are $\sim$5 nm RE_2O_3 arrays, as shown in (b) and (f). In comparison to A and C, BHO precipitate in B are less dense. Instead, they are 3–40 nm in size and randomly distributed. Also, some of them are slightly elongated along the *c*-axis, forming very short nanorods of $\sim$10 nm in diameter. Both of them are potential pinning centers, as shown in Fig. 4(d).

Fig. 5 presents χ-φ XRD pole figures (PF) of REBCO (003) and (103) diffraction to compare the out-of-plane and the in-plane texture. All 3 CCs show strong in-plane and out-of-plane

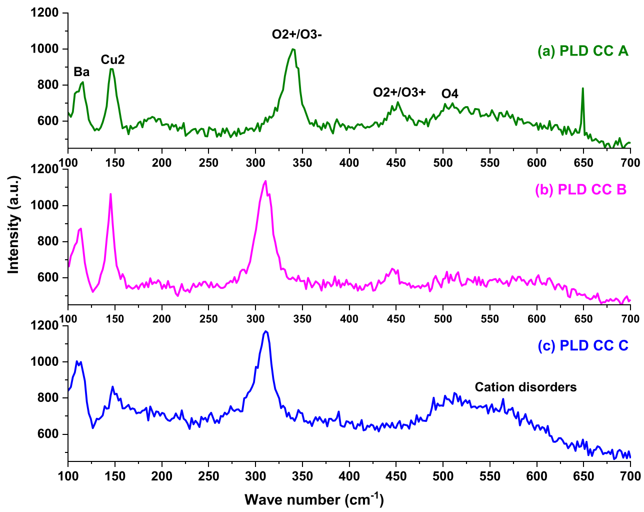

Fig. 6. Raman spectra for (a) A, (b) B, and (c) C. The shoulder at 570–590 cm^{-1} shown by C suggests the presence of cation disorder.

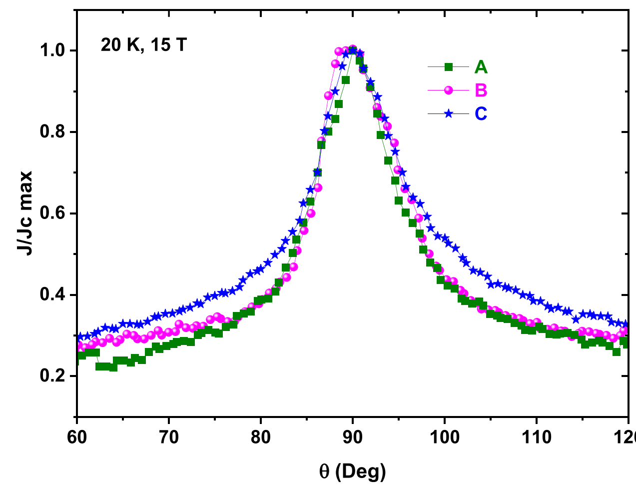

Fig. 7. Normalized angular dependent $J_c(\theta)$ data from Fig. 3. It is interesting that A and B now have almost identical shape while the coated conductor C, almost identical in the range ±5° then adds considerable J_c away from the *ab*-planes.

texture, evidenced by their sharp and distinct peaks. As shown in Fig. 5(a), (b) and (c), the (003) PF peak shows offset from the center of pole figure. The offset in coated conductor A appears along the tape width direction. On the other hand, B and C show the pronounced offset along the length direction although the offset along the tape width direction is smaller than A. Consistent with the (003) shift, the (103) peaks shift to the width and length directions accordingly. In addition to the (003) peak shift, the (103) plane of C rotates 45° along the φ direction, as shown in Fig. 5(f), indicating the [110] direction of REBCO is parallel to the tape length direction.

The overall texture, determined from the (003) and (103) peak angle positions with respect to tilt angle χ, and the corresponding peak width with respect to φ, are listed in the inset table of Fig. 5. According to the table, Conductor A possesses better in-plane texture but larger *c*-axis tilt, while B and C show better out-of-plane texture and smaller *c*-axis tilts.

Fig. 6 compares the Raman spectra [22]. The small peak at 570–590 cm^{-1}, shown by C, signals the presence of cation disorder. No discernible signals of cation disorder were observed on A and B under these test conditions.

IV. Discussion

The $J_c(\theta)$ measurement at low temperatures and high fields has been challenging for REBCO CC characterization, even though the variation of J_c near the *ab*-plane is of high importance for many HTS magnet designs, especially solenoids. By converting $J_c(\theta)$ from the large torques generated by the very high J_c near the *ab*-plane, the torque magnetometer successfully addressed this challenge [19]. For this study, we acquired $J_c(\theta)$ at 20 K and 15 T that is relevant to magnet operation conditions for fusion magnets.

The *ab*-plane offset away from the tape plane for MOCVD CCs has been well described [23]. This offset originates from the IBAD processing to make the textured MgO template for the subsequent highly textured buffers and REBCO layers. Our pole figures in Fig. 5 show this to be present in PLD CCs, which is of course to be expected since all use a similar IBAD MgO template. However, the actual offsets vary from manufacturer to manufacturer. Our recent contemporary study of the length-wise offset confirms this variability and shows that at least for one manufacture the offset can have both short length and a meandering variability [24]. Perhaps not surprisingly, we find that this *ab*-plane offset correlates directly to the $J_c(\theta)$ peak shift shown in Fig. 3. The *ab*-plane offsets, according to pole figure measurements, are ∼4° for conductor A, ∼0.5° for B and ∼0.25° for C, while the peak $J_c(\theta)$ values are found to be displaced by ∼3.88° for A, ∼0.92° for B and ∼0.32° for C. Given the uncertainties of our pick-up coil measurement of θ, we regard this agreement as good. We continue to work on the instrumentation of our home-built magnetometer and more accurate angle determination is one facet of this development.

XRD pole figure provides more detailed REBCO grain orientation information. We observed that, besides the tilt along the width direction, the *ab*-plane tilts along the CC length direction for conductors B and C, a result that we did not expect. This tilt, similar to the tilt across the width, may affect magnet performance too, especially at tape transitions from one pancake to another in double pancake windings. Although the *ab*-plane shift is general for all CCs utilizing the IBAD buffer process, the variation of offset angles from one conductor to another suggests that it is feasible to be able to manage and perhaps minimize it during CC manufacturing. An encouraging example is the very small offset of ∼0.32° for conductor C.

Fig. 7 shows the Fig. 3 angular J_c data normalized both to the peak J_c and to the angular position of the peak. This normalization emphasizes the great similarity in the pinning effectiveness of the 3 CCs since A and B are now almost identical ±15° around the "real" *ab*-plane, even conductor C then does pick up some J_c as the *c*-axis is approached (note that torque magnetometry becomes insensitive far away from the *ab*-plane which is why both torque and transport are needed for full characterization).

The prediction of J_c from any one domain to other important ones is still in its infancy but the strong self-similarity shown in Fig. 7 is promising for better future predictions.

We were surprised that none of the 3 CCs contain any long length nanorods considering their frequent presence in PLD growth of high J_c REBCO. Their absence might be due to the too high growth rate and low doping level [4]. The TEM images show that the ~5 nm RE_2O_3 precipitate arrays along the *ab*-plane are the dominant pinning centers. Combined with strong intrinsic *ab*-plane pinning, B shows the highest J_c around the *ab*-plane.

$J_c(H//c)$ has long been used for pinning strength analysis [25], [26]. According to the power law $J_c \propto H^{-\alpha}$ shown in Fig. 2, weak pinning is dominating the difference in α for coated conductors B and C. The much higher α values of B and C suggest a stronger contribution of weak point pins than for A. Such weak pinning contributes significant J_c at all angles due to its intrinsic isotropic property.

The sources for the weak pinning can be attributed to oxygen vacancies induced by the strain from RE_2O_3 precipitates [27], [28], [29]. Cation disorder, disclosed by Raman spectral weight at 570 to 590 cm^{-1}, can also provide effective weak pinning centers. The cation disorder also suppresses and broadens the T_c transition, as shown in Fig. 1. The high T_c values shown by coated conductors B and C might be due to RE elements other than Y or to the manipulation of the oxygen doping level [30], [31].

V. Conclusion

We carried out the comprehensive characterizations to compare the microstructure and superconducting properties in the commercially available PLD REBCO CCs. Our work shows that nano-precipitate arrays are the dominant strong pinning centers in those CCs. Even though all REBCO films were grown by PLD, the pinning nanostructure varies from conductor to conductor. However, the normalized $J_c(\theta)$ indicates that the pinning effectiveness is rather similar among those CCs, but the variation of *ab*-plane offset creates distinct difference in J_c dependence on field and temperature. This variation also suggests that presently uncontrolled *ab*-plane offsets may be controllable during manufacturing. As core magnet designs consider the effects of *ab*-plane offsets in magnet design when screening current stresses must be controlled, there may be a need to make this a part of a manufacturing specification.

Acknowledgment

The authors are grateful to discussions with Cade Watson, Nonoko Kametani, Jonathan Lee, Garfield Murphy, Griffin Bradford, Chiara Tarantini, and Lance Cooley, and technical help from Van Griffin and William Starch.

References

[1] A. Molodyk and D. C. Larbalestier, "The prospects of high-temperature superconductors," *Science*, vol. 380, no. 6651, pp. 1220–1222, Jun. 2023, doi: 10.1126/science.abq4137.

[2] B. N. Sorbom et al., "ARC: A compact, high-field, fusion nuclear science facility and demonstration power plant with demountable magnets," *Fusion Eng. Des.*, vol. 100, pp. 378–405, Nov. 2015, doi: 10.1016/j.fusengdes.2015.07.008.

[3] R. F. Vieira et al., "Design, fabrication, and assembly of the SPARC toroidal field model coil," *IEEE Trans. Appl. Supercond.*, vol. 34, no. 2, Mar. 2024, Art. no. 0600615, doi: 10.1109/TASC.2024.3356571.

[4] A. Molodyk et al., "Development and large volume production of extremely high current density $YBa_2Cu_3O_7$ superconducting wires for fusion," *Sci. Reports*, vol. 11, no. 1, Jan. 2021, Art. no. 2084, doi: 10.1038/s41598-021-81559-z.

[5] A. Sykes et al., "Compact fusion energy based on the spherical tokamak," *Nucl. Fusion*, vol. 58, no. 1, Nov. 2017, Art. no. 016039, doi: 10.1088/1741-4326/aa8c8d.

[6] J. L. MacManus-Driscoll and S. C. Wimbush, "Processing and application of high-temperature superconducting coated conductors," *Nat. Rev. Mater.*, vol. 6, pp. 587–604, 2021, doi: 10.1038/s41578-021-00290-3.

[7] T. Puig, J. Gutierrez, and X. Obradors, "Impact of high growth rates on the microstructure and vortex pinning of high-temperature superconducting coated conductors," *Nat. Rev. Phys.*, vol. 6, no. 2, pp. 132–148, Feb. 2024, doi: 10.1038/s42254-023-00663-3.

[8] Y. Wu et al., "Ultra-fast dynamic deposition of $EuBa_2Cu_3O_{7-\delta}$-$BaHfO_3$ nanocomposite films: Self-assembly structure modulation and flux pinning behaviors," *Mater. Des.*, vol. 224, Dec. 2022, Art. no. 111406, doi: 10.1016/j.matdes.2022.111406.

[9] S. Fujita et al., "Flux-pinning properties of $BaHfO_3$-doped EuBCO-coated conductors fabricated by hot-wall PLD," *IEEE Trans. Appl. Supercond.*, vol. 29, no. 5, Aug. 2019, Art. no. 8001505, doi: 10.1109/TASC.2019.2896535.

[10] [Online]. Available: https://eng.famu.fsu.edu/news/5m-advanced-conductor-technology-development-program-work-begins

[11] J. Feighan et al., "Strong pinning at high growth rates in rare earth barium cuprate (REBCO) superconductor films grown with liquid-assisted processing (LAP) during pulsed laser deposition," *Supercond. Sci. Technol.*, vol. 34, no. 4, Feb. 2021, Art. no. 045012, doi: 10.1088/1361-6668/abe18d.

[12] G. Jiang, Y. Zhao, and Y. Wu, "Empowering the 2G-HTS tape industry: SuperMag's progress on production and research," in *Proc. Appl. Supercond. Conf.*, Salt Lake City, CO, USA, Sep. 2024.

[13] [Online]. Available: https://indico.cern.ch/event/1220254/contributions/5270652/attachments/2607617/4504484/2023-03-08_HTS4acc_Holzapfel_upload.pdf

[14] C. Senatore, C. Barth, M. Bonura, M. Kulich, and G. Mondonico, "Field and temperature scaling of the critical current density in commercial REBCO coated conductors," *Supercond. Sci. Technol.*, vol. 29, no. 1, Jan. 2016, Art. no. 014002, doi: 10.1088/0953-2048/29/1/014002.

[15] A. Godeke, "High temperature superconductors for commercial magnets," *Supercond. Sci. Technol.*, vol. 36, no. 11, Oct. 2023, Art. no. 113001, doi: 10.1088/1361-6668/acf901.

[16] H. Bai et al., "The 40 T superconducting magnet project at the national high magnetic field laboratory," *IEEE Trans. Appl. Supercond.*, vol. 30, no. 4, Jan. 2020, Art. no. 4300405, doi: 10.1109/TASC.2020.2969642.

[17] A. Greenberg et al., "Critical current correlations and regressions across the superconducting parameter space of REBCO wires, B‖c," *IEEE Trans. Appl. Supercond.*, vol. 34, no. 5, Aug. 2024, Art. no. 6602105, doi: 10.1109/TASC.2024.3360937.

[18] A. Francis, D. Abraimov, Y. Viouchkov, Y. Su, F. Kametani, and D. C. Larbalestier, "Development of general expressions for the temperature and magnetic field dependence of the critical current density in coated conductors with variable properties," *Supercond. Sci. Technol.*, vol. 33, no. 4, Feb. 2020, Art. no. 044011, doi: 10.1088/1361-6668/ab73ee.

[19] J. Jaroszynski et al., "Rapid assessment of REBCO CC angular critical current density $J_c(B, T = 4.2\text{ K}, \theta)$ using torque magnetometry up to at least 30 tesla," *Supercond. Sci. Technol.*, vol. 35, no. 9, Aug. 2022, Art. no. 095009, doi: 10.1088/1361-6668/ac8318.

[20] A. Gurevivh, "Pinning size effects in critical currents of superconducting films," *Supercond. Sci. Technol.*, vol. 20, no. 9, pp. S128–S135, Aug. 2007, doi: 10.1088/0953-2048/20/9/S03.

[21] D. R. Nelson and V. M. Vinokur, "Boson localization and correlated pinning of superconducting vortex arrays," *Phys. Rev. B*, vol. 48, pp. 13060–13097, Nov. 1993, doi: 10.1103/PhysRevB.48.13060.

[22] K. Venkataraman, R. Baurceanu, and V. A. Maroni, "Characterization of $MBa_2Cu_3O_{7-x}$ thin films by Raman microspectroscopy," *Appl. Spectrosc.*, vol. 59, no. 5, pp. 639–649, May 2005, doi: 10.1366/0003702053945958.

[23] J. Lu, Y. Xin, Y. Zhang, and H. Bai, "ab-plane tile angles in REBCO conductors," *IEEE Trans. Appl. Supercond.*, vol. 33, no. 5, Aug. 2023, Art. no. 6600504, doi: 10.1109/TASC.2023.3236258.

[24] J. Lee, J. Bang, G. Bradford, D. Abraimov, E. Bosque, and D. Larbalestier, "Lengthwise characterizations of crystallographic tilt in contemporary REBCO coated conductors," *IEEE Trans. Appl. Supercond. Conf.*, vol. 35, no. 5, Aug. 2025, Art. no. 6600605, doi: 10.1109/TASC.2024.3505115.

[25] C. J. van der Beek et al., "Strong pinning in high-temperature superconducting films," *Phys. Rev. B*, vol. 66, Jul. 2002, Art. no. 024523, doi: 10.1103/PhysRevB.66.024523.

[26] J. Gutierrez et al., "Strong isotropic flux pinning in solution-derived $YBa_2Cu_3O_{7-x}$ nanocomposite superconductor films," *Nat. Mater.*, vol. 6, pp. 367–373, May 2007, doi: 10.1038/nmat1893.

[27] A. Xu, V. Braccini, J. Jaroszynski, Y. Xin, and D. C. Larbalestier, "Role of weak uncorrelated pinning introduced by $BaZrO_3$ nanorods at low-temperature in (Y, Gd)$Ba_2Cu_3O_x$ thin films," *Phys. Rev. B*, vol. 86, no. 11, Sep. 2012, Art. no. 115416, doi: 10.1103/PhysRevB.86.115416.

[28] A. Xu, J. Jaroszynski, F. Kametan, and D. C. Larbalestier, "Broad temperature range study of J_c and H_{irr} anisotropy in $YBa_2Cu_3O_x$ thin films containing either Y_2O_3 nanoparticles or stacking faults," *Appl. Phys. Lett.*, vol. 106, Feb. 2015, Art. no. 052603, doi: 10.1063/1.4907891.

[29] C. Cantoni et al., "Strain-driven oxygen deficiency in self-assembled, nanostructured, composite oxide films," *ACS Nano*, vol. 5, no. 6, pp. 4783–4789, May 2011, doi: 10.1021/nn2007628.

[30] J. G. Lin, C. Y. Huang, Y. Y. Xue, C. W. Chu, X. W. Cao, and J. C. Ho, "Origin of the *R*-ion effect on Tc in $RBa_2Cu_3O_7$," *Phys. Rev. B*, vol. 51, no. 18, pp. 12900–120903, May 1995, doi: 10.1103/PhysRevB.51.12900.

[31] R. J. Cava, B. Batlogg, C. H. Chen, E. A. Rietman, S. M. Zahurak, and D. Werder, "Oxygen stoichiometry, superconductivity and normal-state properties of $YBa_2Cu_3O_{7-\delta}$," *Nature*, vol. 329, pp. 423–425, Oct. 1987, doi: 10.1038/329423a0.